Article

Coelectrodeposition of Ternary Mn-Oxide/Polypyrrole Composites for ORR Electrocatalysts: A Study Based on Micro-X-ray Absorption Spectroscopy and X-ray Fluorescence Mapping

Benedetto Bozzini [1,†,*], **Patrizia Bocchetta** [1,†] **and Alessandra Gianoncelli** [2,†]

[1] Dipartimento di Ingegneria dell'Innovazione, Università del Salento, via Monteroni, 73100 Lecce, Italy; E-Mail: patrizia.bocchetta@unisalento.it

[2] Elettra—Sincrotrone Trieste S.C.p.A. S.S. 14, km 163.5 in Area Science Park, 34149 Trieste-Basovizza, Italy; E-Mail: alessandra.gianoncelli@elettra.eu

[†] These authors contributed equally to this work.

[*] Author to whom correspondence should be addressed; E-Mail: benedetto.bozzini@unisalento.it; Tel.: +39-832-297-323; Fax: +39-832-297-111.

Abstract: Low energy X-ray fluorescence (XRF) and soft X-ray absorption (XAS) microspectroscopies at high space-resolution are employed for the investigation of the coelectrodeposition of composites consisting of a polypyrrole(PPy)-matrix and Mn-based ternary dispersoids, that have been proposed as promising electrocatalysts for oxygen-reduction electrodes. Specifically, we studied Mn–Co–Cu/PP, Mn–Co–Mg/PPy and Mn–Ni–Mg/PPy co-electrodeposits. The Mn–Co–Cu system features the best ORR electrocatalytic activity in terms of electron transfer number, onset potential, half-wave potential and current density. XRF maps and micro-XAS spectra yield compositional and chemical state distributions, contributing unique molecular-level information on the pulse-plating processes. Mn, Ni, Co and Mg exhibit a bimodal distribution consisting of mesoscopic aggregates of micrometric globuli, separated by polymer-rich ridges. Within this common qualitative scenario, the individual systems exhibit quantitatively different chemical distribution patterns, resulting from specific electrokinetic and electrosorption properties of the single components. The electrodeposits consist of $Mn^{3+,4+}$-oxide particles, accompanied by combinations of Co^{0}/Co^{2+}, Ni^{0}/Ni^{2+} and $Cu^{0,+}/Cu^{2+}$ resulting from the

alternance of cathodic and anodic pulses. The formation of highly electroactive $Mn^{3+,4+}$ in the as-fabricated material is a specific feature of the ternary systems, deriving from synergistic stabilisation brought about by two types of bivalent dopants as well as by galvanic contact to elemental metal; this result represents a considerable improvement in material quality with respect to previously studied Mn/PPy and Mn-based/PPy binaries.

1. Introduction

The synthesis of nanoparticulate polymer-matrix composites has been the object of active investigation for over two decades and several diverse applications are being proposed, among which electrocatalysis (e.g., [1]) and batteries (e.g., [2]) are prominent fields. Electrochemical methods offer the possibility of performing this type of composite synthesis in a variety of modes, also allowing template-free nanostructuring and surfactantless, *in situ* nanoparticle synthesis. Moreover, the possibility of growing films rather than powders, as in the chemical polymerization approach, allows better morphological and chemical control, with the possibility of producing high-purity materials. In particular, metal/conductive polymer (M/CP) nanocomposites can be electrodeposited by three main approaches: (i) polymer electrodeposition from a bath containing both monomer and metal ions; (ii) electrodeposition of the pure polymer, followed by metal electroplating; (iii) incorporation of independently synthesized nanoparticles during electropolymerization.

In this work, we shall concentrate on the first approach—that for simplicity we shall denominate coelectrodeposition (CECD), giving rise either to the direct deposition of the metal particles onto the growing polymer layer (a typical example is e.g., [3]) or to the entrapment of—typically anionic, (exclusively anionic in the case of pure PPy)—metal complexes that yield metal particles during a subsequent reduction step (e.g., [4]). It has been recently demonstrated that suitable co-polymers of PPy, such as PPy-PSS (Polystyrene sulphonate), can capture cations [5]. Both variants of CECD are expected to result in a 3D, ideally homogeneous, dispersion of metal particles in the polymeric matrix. It should be noted that the electroreduction of metal ions does not exclusively result in crystallization, but can also yield the chemical stabilization of metal species within the polymer layer [6,7], such as the interaction of partially reduced metal ions, e.g., $Cu^{\delta+}$ or $Au^{\delta+}$, to specific (typically N or S) sites of the polymer chains, giving rise to the formation of metal/polymer complexes. It is also worth noting that recently, exclusively cathodic processes have been demonstrated for the CECD of metal/polypyrrole (M/PPy) systems (Sn/PPy [8], $Ni(OH)_2$/PPy [9]). In fact, it is possible to generate cathodically compounds that are able to polymerize pyrrole; specifically, cathodic polymerization of PPy has been used to grow pure polymer nanowire films [10], opening up new opportunities for nanostructuring [2,11].

Key mechnicistic aspects of coelectrodeposition: The doping/dedoping transition—A crucial aspect of composite plating of metals and CPs is that the latter materials are generally doped and conducting under anodic conditions (both during electropolymerization and in contact with electrolytes containing doping anions), while under the cathodic polarization typical of metal electrodeposition they de-dope

and become insulating. This metal-to-insulator transition is commonly explained in terms of percolation between electronically conducting islands embedded in an amorphous non-conducting matrix. Such a transition depends on polymer properties, among which the most significant ones seem to be: type of counter-ion, doping level and degree of structural disorder. These processes can be rationalized effectively within the semi-empirical framework of the Electrochemically Stimulated Conformational Relaxation (ESCR) model proposed in [12] and references therein; briefly: anodic polarization of a PPy film generates localized radical cations along the polymeric chains, resulting in electrostatically driven conformational changes associated with an increase of free volume. In order to ensure electroneutrality, anions are attracted into the polymeric network and their penetration is favored by the matrix expansion. When, instead, a cathodic polarization is applied, the polymer expels the anions and the film shrinks, eventually becoming closed and trapping the counterions that stabilize the charge carriers of the polymer backbone. Of course, de-doping kinetics depends on the instantaneous diffusion coefficient that, in turn, depends on the instantaneous degree of shrinking. According to this mechanism, in principle, the choice of appropriate cathodic conditions and accurate consideration of the capacitive transients, allow to apply the reducing conditions in such a way that the required amount of metal can be plated before the de-doping transient is completed. Moreover, the progressive change of CP electronic conductivity taking place during transient de-doping can be exploited to control the relative nucleation and growth processes, offering an additional handle for particle morphology tailoring [13]. Moreover, it has been shown that deep reduction of PPy can result in the stabilization of the conductivity, probably owing to enhanced trapping of counterions by structural shrinking and closure [14]: this finding has been used for the metallization of such deeply reduced PPy substrates, but in principle it could also find applications in CECD.

Since non-noble metals of technological interest, such as: Co, Ni, Fe, Cu, and Zn tend to become oxidized during the polymerization period, metal oxidation during the anodic processing step—in dependence on the details of electrochemical program and electrolyte chemistry—can have either beneficial or detrimental effects. The former case corresponds generally to the growth of oxides of potential functional interest, e.g., in catalysis [13,15] or corrosion protection, the latter instead to the redissolution of the metal or to the formation of inactive solid species such as hydroxides or basic salts.

Effect of PPy conductivity on metal electroreduction/metal structure and morphology—So far we have highlighted the impact of CP electronic conductivity on the CECD of M/CPs, this aspect is, however, only one of the CP characteristics that is important for metal particle deposition. In fact, in the case of a highly electronically conductive, oxidized and pinhole-free CP layer, metal electrodeposition preferentially occurs at the polymer surface. Nevertheless, in the case of a partially de-doped polymer layer, the CP porous structure and geometrical defectivity, determining ion transport into the bulk of the polymer layer down to the underlying metal electrode surface, will control the metal electrodeposition step, as clearly pinpointed in [16]. In fact, the structure of electrodeposited M/CP composites—and in particular the morphology and space distribution of the metallic components—is the result of the competition between the reduction of metal ions on the surface or inside the polymer layer, on the one hand, and on the underlying metal surface on the other hand.

Electrical parameters of coelectrodeposition—As hinted at above, typically, polymer electrodeposition is performed under anodic conditions and metal deposition under cathodic ones. In the case of metal oxide electrodeposition, in principle the process can be carried out under either

cathodic or anodic conditions. In the most general case, however, M/PC CECD implies the alternation of anodic and cathodic periods that can be applied by several methods, the most straightforward of which are cyclic voltammetry (CV) and reverse pulse-plating (RPP). The CV method is less flexible in the choice of operating parameters, being constrained by sequential access to a range of potentials defined by fixing the terminal ones—typically dictated by the stability of the composite components; once these values have been chosen, the scan rate is the only residual variable. The RPP method, instead, offers a broader range of free deposition parameters and allows the selection of individual potentials or current densities, in combination with fast switching between couples of different, independently optimized plating conditions; in particular RPP gives the possibility of tuning separately the amounts of polymer and metal deposited at each cycle. Moreover, better control over mass-transport conditions is possible thanks to the possibility of defining a pulsating compositional double layer and of relaxing the double layer with zero-current periods. It is worth noting that, in the limit of long deposition periods at a given potential, multilayer M/PPy can be deposited [17]. For an insightful understanding of RPP in M/CP CECD, one should take into account that the current associated with each potential step contains both capacitive and faradaic contributions. At the beginning of the CECD process, the capacitive contribution is exclusively related to the electric double layer charging at the bare electrode surface. However, during the growth of the electroactive composite, a time-dependent pseudocapacitive component develops, due to the variation of the oxidation level of both the polymeric and oxidized metallic materials. As far as the choice of electrical control is concerned, potentiostatic experiments (under the simplifying hypothesis of a constant electroactive area) run at constant overvoltage, facilitating secondary nucleation and typically resulting in tendentially monodisperse metal particles of a single morphology. To the contrary, galvanostatic control intrinsically implies a varying local overvoltage, generally giving rise to a variety of particle sizes and growth shapes.

Experimental methods used for the study of CECD processes and co-electrodeposited materials—A host of analytical methods can be used for the investigation of coelectrodeposited composites, in the following we list them for reference and comparison with the approach proposed in the present paper. In this section we omit details on classical morphological (SEM, TEM), structural (XRD, SAED) and electrochemical (CV, LSV, chronocoulometry) methods as well as on dedicated functional characterizations and rather concentrate on methods that have been chosen specifically for the study of the intrinsic properties of pure PPy films and PPy-matrix composites. (i) AES with depth profiling for the assessment of particle localization within the CP matrix [18]; (ii) AFM for the quantification of homogeneity, grain size and surface roughness (in situ Au/PPy [19]); (iii) DTA and TGA for thermal stability analyses [20]; (iv) EPR for studies of polaronic conduction mechanisms [21] and electronic interactions bewteen PPy matrix and oxide dispersoids [22]; (v) EQCM for the *in situ* monitoring of electropolymerization and composite electrodeposition processes [23] and for the study of ion fluxes into and out of electropolymerized films [5,24,25]; (vi) ERS [26,27] and spectroellipsometry [28] for the definition of charge-transfer processes during both electropolymerization and electrocatalysis; (vii) FTIR and Raman, for the investigation of the interaction between PPy matrix and oxide particles (FTIR Fe_2O_3 [20], FTIR TiO_2 [29], FTIR Fe–Co/PPy [30], ATR-IR Cu basic salts [5], Raman Fe_3O_4 [31], Raman SnO_2 [2]); (viii) ICP-AES for the analysis of the metal content in PPy-matrix composites (Sn [2]); (ix) NEXAFS [32] for a detailed study of charge transfer between Co and PPy; (x) Solid state electrochemical impedance for the differential evaluation of the electrical resistance of films [31];

(xi) UV spectroscopy was used for the study of the electronic structure of PPy and of the way the presence of particles modifies it [33]; (xii) XPS with depth profiling revealed the chemical state of inorganic dispersoid (Fe in prussian blue/PPy CECD [34], Sn in SnO_2/PPy [10], Cu and S in $Cu_x(OH)_y(SO_4)_z$ [5], Cu and N in SO_4–Cu/PPy [35], Pt and Ru [4]) and allowed the assessment of the chemical interaction of the dispersoid with the matrix (chiefly by N 1s spectroscopy [5,10,35]).

Literature on coelectrodeposition—In the otherwise vast literature on the electrodeposition of M/CP composites, only a comparatively limited number of papers deals with CECD in the strict sense. M/CP CECD can be classified into two main categories, according to the nature and chemical state of the metal component: (i) noble metals; (ii) reactive metals and oxides. In the following, we shall briefly review the M/PPy systems that are directly relevant to the present work. We emphasize that the specific focus of the present paper is on type (ii) systems, since our aim is to coelectrodeposit reactive metals, that either in their elemental or oxide forms are expected to be efficient ORR electrocatalysis in alkaline environments. Thus, below, we report a list of M/PPy composites grown by CECD. (i) Noble metals—(i.a) Au/PPy: a peculiar RPP waveform was proposed in [3], combining the effects of pulse-plating with deposition interruption and polarization reversal for CECD. In fact, CECD leads to improved layer smoothness and homogeneity as well as finer Au grains in comparison with DC plating of similar materials. (i.b) Pt/PPy: sandwich composites, consisting of multiple electrodeposited PPy and Pt layers have been studied in [17]. (i.c) The growth of Ir, Pd, Pt and Ru/PPy composites has been described in [4], as obtained by polymerization in the presence of anionic Pt-group complexes that were reduced in a post-treatment, applied after completion of the polymer growth phase. This approach is not strictly CECD in the sense defined above, but it is closely related to it in that a single bath containing both pyrrole and a metal salt was employed. (ii) Reactive metals—(ii.a) Co/PPy: the synthesis from a single Co-pyrrole bath by two-step anodic-cathodic polarization is reported in [32]; CECD from an acetonitrile bath for the fabrication of ORR electrocatalysis is expounded in [36]; in [37] the same system has been studied by applying a complex anodic-cathodic pulse sequence: this work is chiefly focused on Co/PPy composites, but some results are also reported on Mn/PPy and Fe/PPy; (ii.b) PPy/SO_4–Cu [35] CECD has also been regarded as an improvement of two-step processes, able to yield finer dispersions of Cu without pore-clogging. (ii.c) Fe/PPy: grown by potentiostatic RPP has been shown to allow the combination of the peculiar magnetic properties of matrix and dispersoid [38]. (ii.d) Ni/PPy: RPP, with a detailed analysis of the impact of pulse parameters on composite film properties, has been studied in [39]. To the best of the authors' knowledge, the only papers published so far on alloy/PPy CECD are [30,40,41]. In [30] CECD of Fe–Co/PPy is reported as a fabrication route for composite coaxial nanowires; these materials, that exhibit interesting magnetic properties, have been electrodeposited from an aqueous sulphate solution into appropriate templates, by employing sinusoidal AC at 50 Hz with an amplitude 13.3 V. From the point of view of the CECD mechanism, the authors claim that the coaxial structure is the result of enhanced PPy nucleation at the template surface. CECD of Mn–Co/PPy, in conjunction with *in situ* by XRF mapping and micro-XAS spectroscopy, is described in [40]. A detailed space-resolved XRF study of Mn–Cu–Mg/PPy composites is illustrated in [41], accompanied by mathematical modelling of the experimentally observed electrodeposition patterns. By inspection of the relevant literature, one can conclude that—not only in the specific field of CECD, but more in general in M/CP electrodeposition—despite numerous studies and persistent research interest, most of the works

describe the relevant process with a multiplicity of phenomenological approaches often with ill-specified characteristics, thus providing a poor basis for comparison among the results of different investigations. It is the authors' opinion that it is currently difficult to gain a general understanding and consequently of controlling the characteristics of the composites, especially in terms of composition, chemical state, number, size, and spatial distribution of the electrodeposited metal crystals. We therefore reckon that the systematic use of complementary multitechnique *ex situ* [41], quasi *in situ* [15] and *in situ* [42] microspectroscopic tools is required for next generation studies of these systems.

In the present paper, we have concentrated on electrochemical fabrication of ternary, Mn-based composites for alkaline ORR electrocatalysts. The background to this study is the replacement of expensive and scarce platinum by non-noble metals for the catalysis of the oxygen reduction reaction (ORR). ORR in alkaline media is a fundamental cathodic reaction in polymer membrane electrolyte fuel cells and metal–air batteries [43]. Among the different materials proposed, a highly attractive class of electrocatalysts is the non-precious metal/polypyrrole system (e.g., [15,41,42,44,45] and references therein). Polypyrrole is an excellent matrix for ORR catalysts for several reasons: (i) its relatively high nitrogen content, that allows the formation of ORR active Me-N sites within the intact polymer structure; (ii) reasonable environmental stability and relatively good robustness with respect to peroxide attack; (iii) high electrical conductivity [46]; (iv) optimal adhesion of catalyitic oxides [47]. These aspects are key to ensuring ORR-active and stable triple phase boundaries with optimal electrical contact to the electronically nonconductive metal oxide catalyst particles. Moreover, polypyrrole offers the advantage of an easy chemical [48] or electrochemical [49] synthesis. We selected Mn-based materials because of their well-known properties as an ORR electrocatalyst for alkaline systems [50–52]: high catalytic activity with the capability to decomposing hydrogen peroxide, environmental compatibility and low cost. Our choice of ternary systems intends to address two mechanisms of electrocatalytic enhancement: (i) stabilization of the Mn-based oxygen mediator species by doping with Co, Mg, and Ni; (ii) achievement of dual-function behavior by dispersing metallic nanoparticles. Doping with low-valent elements such as Co, Mg, and Ni has been reported to enhance the catalytic activity of MnO_x toward ORR [53,54]. On the one hand, Mn^{4+} and Mn^{3+} species are regarded as oxygen mediators for oxygen reduction in the 4-electron pathway and their coexistence—that has been shown to be favored by doping with divalent cations—is believed to assist the charge transfer to molecular oxygen and thus facilitate the ORR [54]. On the other hand, combining metal nanoparticles with MnO_2 has been reported to favor the 4-electron pathway as well as the peroxide scavenging action [55].

The synthesis of Mn–Co–Cu/PPy, Mn–Co–Mg/PPy and Mn–Ni–Mg/PPy composites was performed by anodic-cathodic pulse-plating from an acetonitrile bath. During the anodic pulse the electropolymerization takes place together with the insertion of Mn^{2+} coordinated by pyrrolic nitrogen and the anodic oxidative deposition of Mn^{3+}, Mn^{4+} oxide, while the cathodic pulse potentially precipitates metallic and colloidal manganese hydroxide nanoparticles onto the undoped polymer. The morphochemical properties of the composite electrocatalyst resulting from electrochemical deposition were assessed by soft X-ray fluorescence and absorption microspectroscopy.

2. Results and Discussion

The three investigated types of composites exhibit characteristic STXM morphologies (Figure 1), resulting from the electrokinetic details of the single electrodeposition systems (see, e.g., [40,41]), an insightful determination of which is beyond the scope of the present paper. STXM images bear absorption contrast information from the whole thickness of the sample, convolving—according to the Beer-Lambert law—local optical path and compositional information. From soft X-ray absorption it is possible to estimate that the thicknesses of our samples vary in the range 100 ÷ 400 nm. Mn–Co–Cu/PPy (Panel A) exhibits a homogeneous surface with mesoscopic globuli; Mn–Co–Mg/PPy (Panel B) shows a combination of micrometric polymer flakes with micrometric globular structures and Mn–Ni–Mg/PPy (Panel C) features mesoscopic patches. All the investigated materials consist of approximately monodisperse isolated polymer-rich islands, the dimensions of which are smallest in Mn–Co–Mn/PPy (*ca.* 3 μm), intermediate in Mn–Co–Cu/PPy (*ca.* 7 μm) and largest in Mn–Ni–Mg/PPy (*ca.* 10 μm).
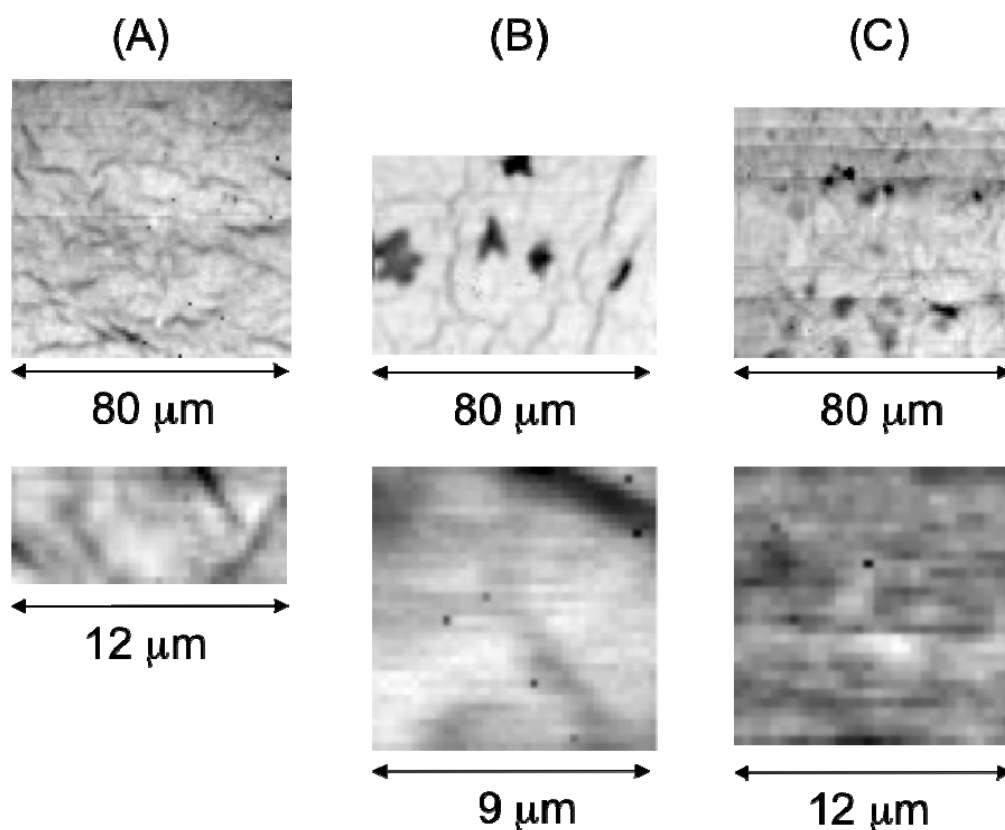

Figure 1. STXM images of electrodeposited Mn-based/PPy composites: (**A**) Mn–Co–Cu/PPy (energy: 1 keV, step size: top 1 μm, bottom 0.3 μm); (**B**) Mn–Co–Mg/PPy (energy: 1.4 keV, step size: top 1 μm, bottom 0.3 μm); (**C**) Mn–Ni–Mg/PPy (energy: 1.4 keV, step size: top 1 μm, bottom 0.3 μm).

2.1. ORR Electrocatalytic Activity

The electrocatalytic activity towards ORR of Mn–Co–Cu/PPy, Mn–Co–Mg/PPy and Mn–Ni–Mg/PPy electrodeposited composites was investigated by determining the quasi-steady-state

voltammograms at a scanning rate of 5 mV s^{-1} in O$_2$-saturated 0.1 KOH aqueous solutions at different RDE rotation speeds (Panels A, B and C of Figure 2). The apparent key electrocatalytic parameters (ORR current density, onset potential and half-wave potential) are reported in Table 1.
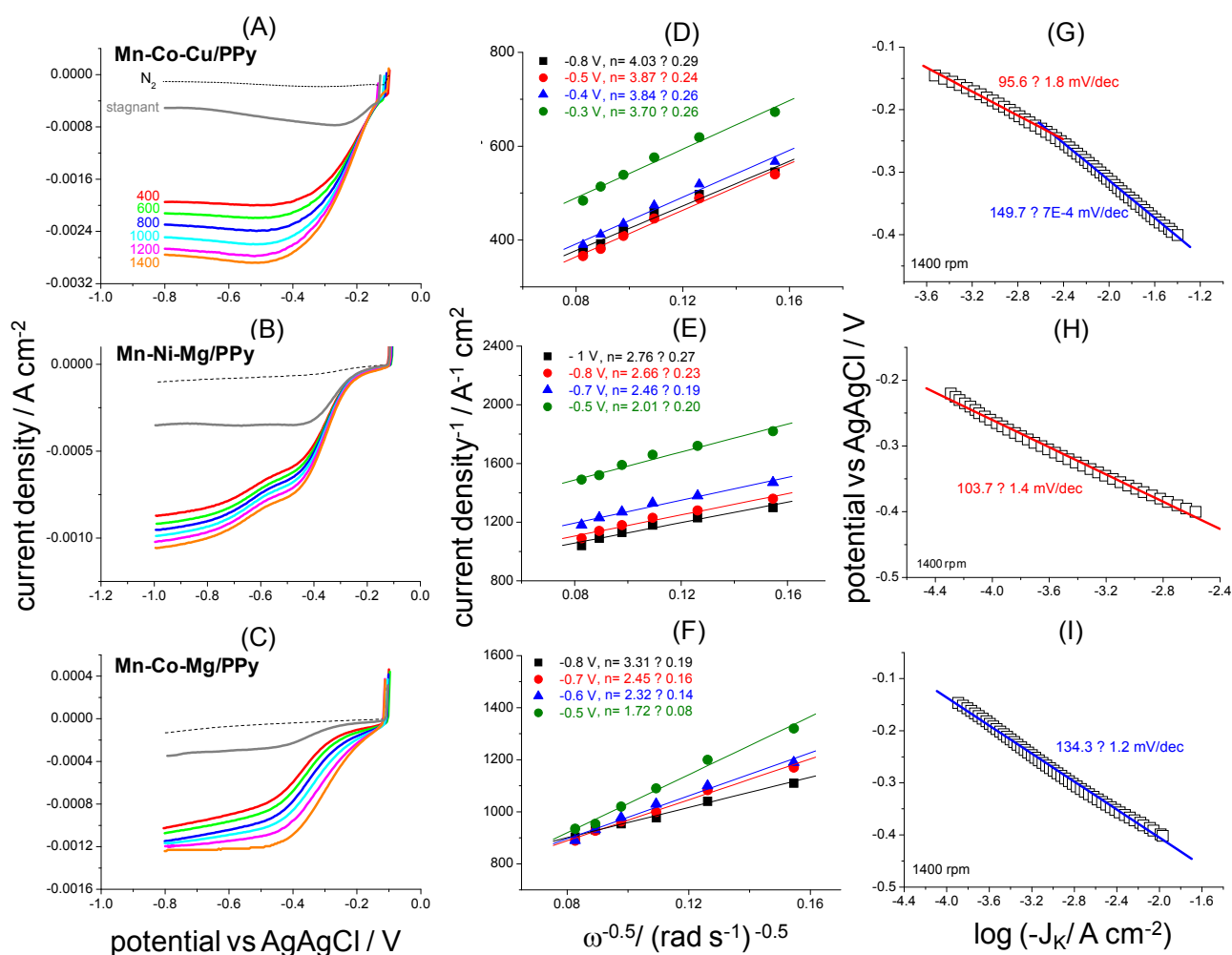

Figure 2. (**A**,**B**,**C**) RDE voltammograms recorded with Mn–Co–Cu/PPy, Mn–Ni–Mg/PPy and Mn–Co–Mg/PPy electrocatalysts in N$_2$- and O$_2$-saturated 0.1 KOH solution at 5 mV s^{-1} and different RDE rotation rates (see Panel A). (**D**,**E**,**F**) Corresponding Koutecky-Levich plots at the indicated electrode potentials. (**G**,**H**,**I**) Tafel plots from ORR cyclovoltammetric curves recorded at 1400 rpm.

Table 1. ORR electrocatalytic parameters for Mn–X–Y/PPy composites from voltammograms recorded in 0.1 M KOH with an RDE at 1400 rpm.

Electrocatalyst	$E_{1/2}$/V	E_{onset}/V	J at 0.3 V/mA cm^{-2}	J_L/mA cm^{-2}
Mn–Co–Cu/PPy	−0.22	−0.122	−2.23	−2.87
Mn–Ni–Mg/PPy	−0.34	−0.237	−0.213	−0.74
Mn–Co–Mg/PPy	−0.28	−0.148	−0.75	−1.2

The electrocatalytic parameters are optimal for the Mn–Co–Cu/PPy electrodes, while they drastically decrease when cobalt is not present in the catalyst (Mn–Ni–Mg/PPy).

The electron transfer number (*n*) was determined by using the Koutecky-Levich equations [56]:

$$\frac{1}{j} = \frac{1}{j_L} + \frac{1}{j_K} = \frac{1}{B\sqrt{\varpi}} + \frac{1}{j_K} \qquad (1)$$

$$B = 0.62nFC_o \left(D_o\right)^{\frac{2}{3}} v^{-\frac{1}{6}} \qquad (2)$$

where J_K is the kinetic current density, J_L the diffusion-limiting current density, J the measured current density, B the reciprocal of the slope, ϖ the angular velocity of the disk ($\varpi = 2\pi N$ with N the linear rotation speed), F the Faraday constant, C_o the saturated concentration of O_2 in 0.1 M KOH at room temperature (1.2×10^{-6} mol cm^{-3}), D_o the diffusion coefficient of oxygen in water (1.73×10^{-5} cm^2 s^{-1}) and v the kinematic viscosity of the solution at room temperature (0.01 cm^2 s^{-1}) [57].

The Koutecky-Levich plots for the Mn–Co–Cu/PPy, Mn–Co–Mg/PPy and Mn–Ni–Mg/PPy electrocatalysts are reported in Panels D, E, and F of Figure 2, respectively. The slopes of their semilogarithmic fit lines were used to estimate the number of electrons transferred (*n*) according to Equation (2), at different electrode potentials. The value of *n* gradually increases with the increase of the cathodic potential, indicating that the fraction of HO_2^- produced at low overpotentials subsequently reduces to OH^- at more negative potentials. The Mn–Co–Cu/PPy sample favours the 4e$^-$ oxygen reduction process (O_2 is directly reduced to OH^-) in agreement with literature on Mn–Co–Cu oxides [58] and similarly to commercial Pt/C catalyst in the same 0.1M KOH electrolyte [59]. On Mn–Co–Mg/PPy and Mn–Ni–Mg/PPy samples, instead, the O_2 reduction follows a combination of 2e$^-$ (reduction of O_2 to HO_2^-) and 4e$^-$ reactions. The comparison in terms of charge-transfer kinetics is better highlighted in the mass-transport corrected Tafel plots of Figure 2 Panels G, H and I, where kinetic current J_K is estimated according to $1/J = 1/J_L + 1/J_K$. For the Mn–Co–Cu/PPy sample, two Tafel regions with slopes of 95.6 and 149.7 mV dec^{-1} can be observed at low and high overpotentials, respectively. This slope variation is generally attributed to the modifications in the surface coverage with adsorbed oxygen [60,61]. According to these results, the combination of Mn, Co and Cu dispersoids into PPy using the electrodeposition protocol described in this paper, results in the best electrocatalytic activity towards ORR. Of course the ORR efficiency depends not only on the nature of the metals, but it is a system property [58]. Since as-formed PPy is ORR inactive [37], the knowledge of the metal chemical state inside the polymeric matrix and its correlation with the electrodeposition parameters is key to optimising the synthesis process towards more efficient electrocatalysts.

2.2. Characterization of Ternary Mn-Based/PPy Electrodeposited Composites by Low Energy X-ray Fluorescence Microspectroscopy

We recorded XRF maps of electrodeposited Mn–Co–Cu/PPy, Mn–Co–Mg/PPy and Mn–Ni–Mg/PPy composites (Figures 3–5) in representative positions, *i.e.*, in locations of the samples that exhibit a class of morphochemistries that has been assessed to be typical on the basis of series of STXM micrographs acquired at different energies across the relevant absorption edges as well as XRF maps. Moreover, we have selected two magnifications that allow to capture effectively: (i) the microscopic patterns that are typical of pristine conditions (with a spot size of 1 μm in diameter) and (ii) the mesoscopic morphochemical features that develop as a result of ageing (with a spot size of 300 nm in diameter, a good compromise between spatial resolution and significant XRF signal).
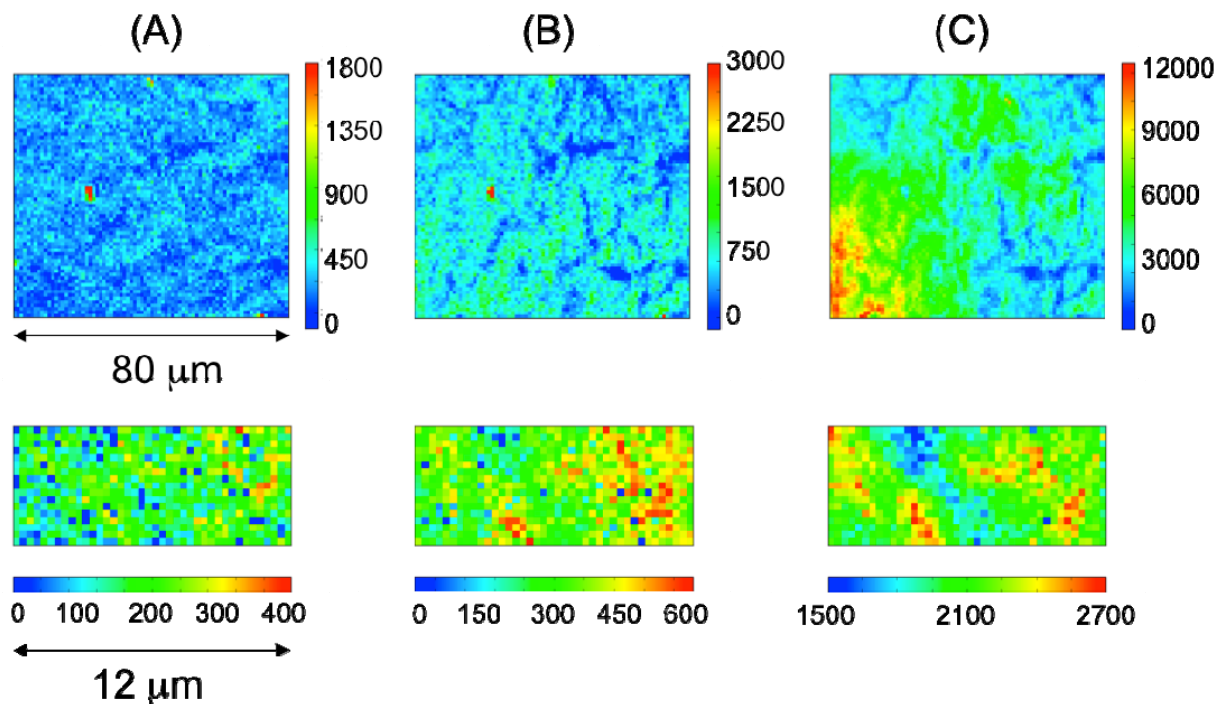
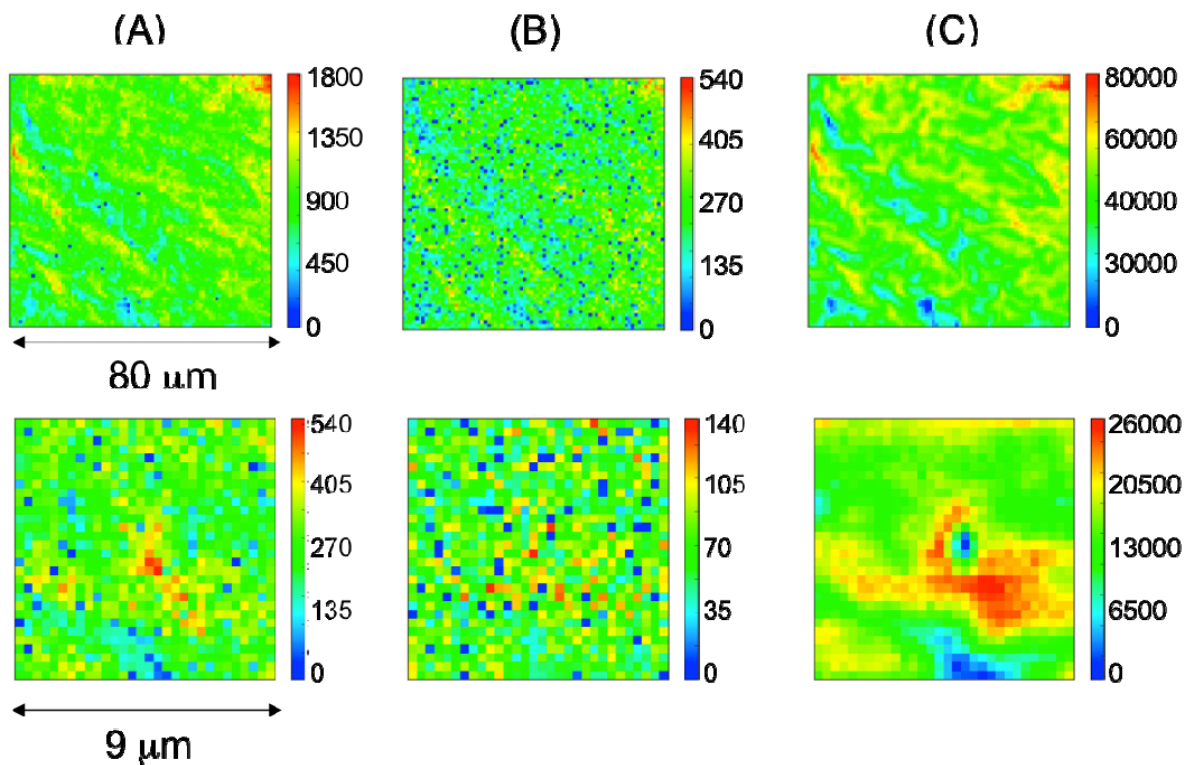**Figure 3.** XRF maps of electrodeposited Mn–Co–Cu/PPy composites (energy: 1 keV, step size: top 1 μm, bottom 0.3 μm): (**A**) Mn; (**B**) Co; (**C**) Cu.

Figure 4. XRF maps of electrodeposited Mn–Co–Mg/PPy composites (energy: 1.4 keV, step size: top 1 μm, bottom 0.3 μm): (**A**) Mn; (**B**) Co; (**C**) Mg.
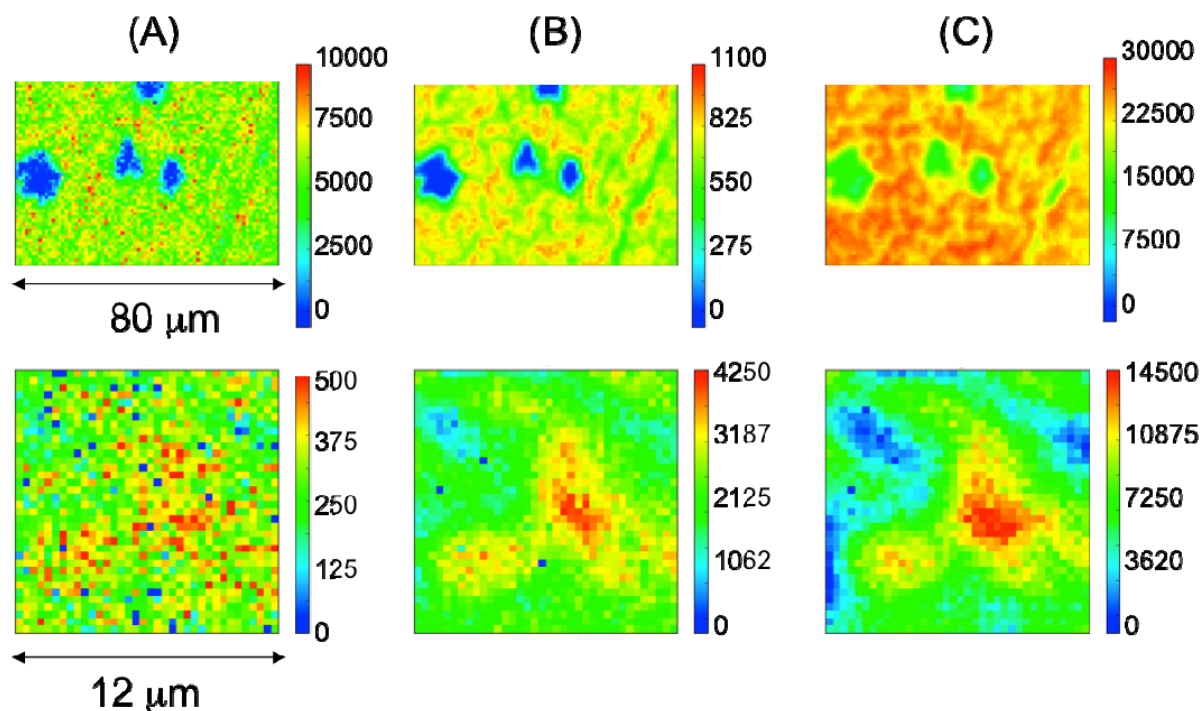
Figure 5. XRF maps of electrodeposited Mn–Ni–Mg/PPy composites (energy: 1.4 keV, step size: top 1 μm, bottom 0.3 μm): (**A**) Mn; (**B**) Ni; (**C**) Mg.

All the investigated materials exhibit common qualitative aspects: (i) the elemental distribution is approximately bimodal, characterized by mesoscopic clusters of micrometric granuli, separated by polymer ridges (showing higher absorption in STXM images in conjunction with lower metal content in XRF maps); (ii) the elements are co-localized in our electrochemically grown composites with the exception of Cu. In fact, Cu is the most electroactive species in our electrodeposition baths and deposits predominantly in a reduced form (see Section 2.3), exhibiting a codeposition behavior that is less coupled to that of the other metallic elements. Besides these common features, the individual materials are characterized by typical subpatterns consisting of aligned assemblies of micrometric grains. These patterns, as well as the morphochemically decoupled behavior of Cu, can be interpreted in terms of a dynamical electrodeposition model, recently developed by some of the authors [62,63] and validated experimentally with XRF maps [41]: a systematic analysis of this topic will be the object of a dedicated paper, but we can anticipate that it is possible to find a set of parameters within the Turing-Hopf region in which the observed patterns can be reconstructed theoretically.

2.3. Characterization of Ternary Mn-based/PPy Electrodeposited Composites by Soft X-ray Micro-XAS Spectroscopy

We measured micro-XAS spectra at the Mn L-edge (Figure 6) as well as at the Co, Cu and Ni L-edges (Figure 7) from Mn–Co–Cu/PPy, Mn–Co–Mg/PPy and Mn–Ni–Mg/PPy electrodeposits in sets of representative positions within the areas of the XRF maps reported in Figures 3–5 and expounded in Section 2.2. Unfortunately, the C absorption edge is not accessible at TwinMic while the quality of XAS spectra at Mg K-edge was not good enough to provide useful spectroscopic information. This is due to the fact that, in order to have a suitable energy resolution, small exit slits are needed, that end up

reducing the flux of the beam by two orders of magnitude and therefore strongly degrade the signal to noise ratio of the absorption spectra. Unless otherwise stated, the reported micro-XAS are the result of averaging five to eight normalized spectra, recorded in different positions with a spot size of around 1 μm. Apart from peculiar cases, that will be pointed out explicitly, in the different sample locations we examined, the spectra turned out to be identical in shape even though different in intensity, of course owing to the presence of different amounts of material as a result of electrochemical pattern formation. Mn spectra (Figure 6) show that the three composites contain Mn essentially in the same chemical form: Mn^{3+} is the dominating species, while variable amounts of Mn^{4+} are found in the single ternary systems and occasionally (see below) in different points of their surface. In particular, the Mg-containing materials (Spectra B and C) feature a homogeneous chemical state content with the same amount of Mn^{4+}, while Mn–Co–Cu exhibits the presence of two types of sites: Cu-richer areas correlate with higher amounts of Mn^{4+} (A, red curve), probably because galvanic coupling to reduced Cu favors the more oxidized form of Mn. Thus, the main differences in ORR activities observed in Section 2.1 can be related to the chemical nature and distribution of the other metals (Co, Ni, Mg) in the Mn/PPy composite.
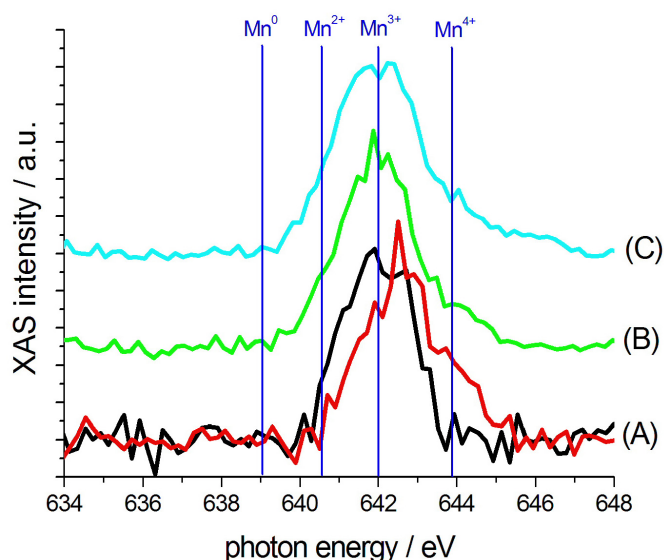

Figure 6. Micro-XAS at the Mn L-edge of electrodeposited Mn-based/PPy composites: (**A**) Mn–Co–Cu/PPy (red plot: high-Cu zones); (**B**) Mn–Co–Mg/PPy; (**C**) Mn–Ni–Mg/PPy.

The predominance of Mn^{3+} and Mn^{4+} in the materials grown in this study is a notable result, because in the ternary systems the CECD process yields directly Mn in its most electrocatalytically active form, while in Mn/PPy and binary Mn-based/PPy materials, non-electrocatalytic forms dominate—Mn^0/Mn^{2+} *in situ* and Mn^{2+} after exposure to ambient air [40]—and can be converted to a mixture of Mn^{3+} and Mn^{4+} only by thermal or electrochemical post-treatments. The stabilization of higher-valent Mn by doping with two-valent cations is expected on the basis of [53,54] and results to be more effective in the case of co-doping in ternary systems rather than by simple doping with a single species; moreover, galvanic coupling provided by Cu^0 turns out to be even more effective in stabilizing the 4-valent form [55].
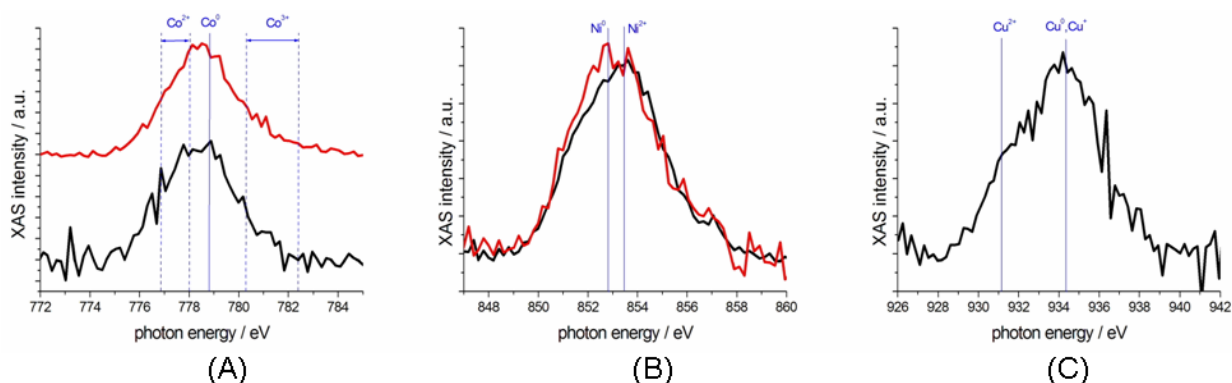
Figure 7. Micro-XAS of electrodeposited Mn-based/PPy composites: (**A**) Co L-edge (black plot: Mn–Co–Cu/PPy, red plot: Mn–Co–Mg/PPy); (**B**) Ni L-edge (Mn–Ni–Mg/PPy. Red plot: high-Ni zones); (**C**) Cu L-edge (Mn–Co–Cu/PPy).

Panel A of Figure 7 reports the Co L-edge spectra obtained by averaging several micro-XAS measured in a range of locations of the surface of Mn–Co–Cu/PPy and Mn–Co–Mg/PPy electrodeposits, and shows that a mixture of Co^0 and Co^{2+} forms, coherently with our results on Co/PPy [15,42] and Mn–Co/PPy [40]. The presence of both valences results from the fact that this element is incorporated into the composite by both electrodeposition and electroprecipitation processes taking place during the cathodic and anodic pulse-plating branches, respectively. Similarly to the Co-containing electrodeposits, Mn–Ni–Mg/PPy shows a mixture of Ni^0 and Ni^{2+} (Figure 7, Panel B). Instead, at variance with Co—the chemical state distribution of which is more homogeneous—micro-XAS at the Ni L-edge shows that the sites exhibiting a higher Ni content also tend to have a higher amount of Ni^0, coherently with the correlation between chemical state and amount of the electrodeposited metallic component pinpointed in [42]. As far as Cu is concerned (Figure 7, Panel C), in the Mn–Co–Cu/PPy composite two states are found: the one at lower photon energy (*ca.* 931.1 eV) can be unambiguously attributed to Cu^{2+} while that at higher energy (*ca.* 934.3 eV) corresponds to a reduced form, either Cu^0 or Cu^+: we can thus conclude that Cu is incorporated in our electrodeposits both as a two-valent dopant and in an electroreduced form generated during the cathodic pulse. By considering that Co L-edge spectra (Figure 7) in several areas of the electrodes show the same chemical distribution in Mn–Co–Cu/PPy and Mn–Co–Mg/PPy, the best ORR activity observed of Mn–Co–Cu/PPy can be correlated to the presence of copper instead of magnesium. It was recently reported that excellent ORR performance in Cu^{2+}-containing catalyst can be related to the imperfections in Cu^{2+} active site configuration induced by adjacent Cu^0/Cu^+ and nitrogen ligands that provide an optimal environment for electronic bonding of O_2 to Cu^{2+} ions [64].

3. Experimental Section

3.1. Materials and Electrodes

Acetonitrile, $MnCl_2 \cdot 6H_2O$, $CoCl_2 \cdot 6H_2O$, $NiCl_2 \cdot 6H_2O$, $CuCl_2 \cdot 2H_2O$, $MgCl_2 \cdot 6H_2O$ and pyrrole were supplied by Aldrich (Sigma Aldrich S.R.L., Milano, Italy). Before each PPy electrodeposition experiment, the pyrrole monomer was distilled under rotary pump vacuum several times (typically three) until it became colorless. All the solutions were prepared with ultrapure water from a MilliQ system

(Millipore, Vimodrone (MI), Italy), exhibiting a resistivity of 18.2 MΩ cm. Electrodeposition and electrochemical measurements were performed using a classical three-electrode cell, with the working electrode held in a hanging-meniscus configuration, a Pt wire spiral (5 cm^2) as counter electrode (CE) and an aqueous silver/silver chloride (Ag/AgCl/3M: 0.209 V/NHE) as reference electrode (RE), connected to the solution by a salt bridge. In electrochemical measurements involving the acetonitrile bath, the liquid junction potential between aqueous and non-aqueous solutions has been checked to be negligible. Nitrogen (SIAD 0.6, SIAD, Bergamo, Italy) was bubbled for 20 min into the solution before every electrochemical measurement. Electrodeposition was performed under a N$_2$ blanket. Au TEM grids (Assing, Monterotondo (Roma), Italy) have been used as support to investigate in detail the electrochemistry and composition of the electrodeposited material by Soft X-ray absorption spectroscopy (XAS) and X-ray Fluorescence (XRF) mapping.

3.2. Coelectrodeposition (CECD) Process

The CECD of Mn–Co–Cu, Mn–Co–Mg and Mn–Ni–Mg with PPy has been performed in de-aerated acetonitrile solutions containing 0.1 M pyrrole, 1% *v/v* H$_2$O, 0.1 M Tetra-Butyl Ammonium Perchlorate supporting electrolyte, 0.017 M MnCl$_2$ and the appropriate combinations of 0.017 M XCl$_2$ (X = Co or Ni) and 0.017 M YCl$_2$ (Y = Mg, Cu). The electrodeposition protocol was a modification of the step pulsed potential method originally proposed in [37] and revised in [15,44], consisting in an initial step at 0 V for 1 s (#1), a subsequent anodic pulse at +1.2 V for 0.5 s (#2), a cathodic step at −1.8 V for 0.5 s (#3) and a final anodic step at +1.2 V for 0.2 s (#4). The potential values have been selected according to the approach discussed in [40,41]. The rationale of this type of cycles is: (i) to grow a composite consisting in principle of two constituents that are formed anodically (PPy, Mn$^{3+,4+}$) and cathodically (M^0) and (ii) to avoid the build-up of large monomer concentration gradients at the electrode/electrolyte interface during electropolymerization on the one hand and to reduce the stripping of metal particles during the anodic pulses on the other hand. The initial step #1 does not lead to faradaic reactions, but it is required to relax the compositional double-layer. After this relaxation step, an anodic layer of Mn$^{3+,4+}$/PPy is electrodeposited during the first anodic pulse #2. As a result of the subsequent cathodic pulse #3, reduced metal species can in principle be incorporated into PPy and in the final anodic step of each cycle #4, another layer of Mn$^{3+,4+}$/PPy is expected to be deposited. The metal EDS compositions, averaged over areas of 100 × 100 μm^2, are: (i) Mn–Co–Cu/PPy, Co 24 ± 3 at. %, Cu 14 ± 5 at. % (balance Mn); (ii) Mn–Co–Mg/PPy, Co 31 ± 5 at. %, Mg 12 ± 4 at. % (balance Mn); (iii) Mn–Ni–Mg/PPy, Co 26 ± 3 at. %, Mg 16 ± 3 at. % (balance Mn).

3.3. ORR Electrocatalytic Activity Evaluation

The electrocatalytic activity of Mn–X–Y/PPy (X = Co, Ni; Y = Mg, Cu) catalysts towards ORR was evaluated by linear sweep voltammetric measurements in O$_2$-saturated (SIAD 6.0) 0.1 M KOH electrolyte under quasi-steady-state conditions (5 mV s^{-1}) at different disc electrode (RDE) rotation speeds. Glassy carbon electrodes with Mn–X–Y/PPy electrodeposit (for details on electrodeposition see Section 3.2) were mounted in a Rotating Disk Electrode System (Parstat Model 2273, Photo Analytical S.R.L., Settala (MI), Italy). The same electrochemical experiments were duplicated with solutions that had been de-oxygenated by N$_2$ saturation. O$_2$ was bubbled for 20 min into the solution

before the measurements and an O_2 blanket was maintained above the electrolyte during voltammetry. The current density values were depurated from the N_2 current contribution before the estimation of electron transfer numbers and Tafel slopes.

3.4. Soft X-ray Absorption and Fluorescence Mapping

Soft X-ray transmission microscopy (STXM), coupled with micro-spot X-ray absorption spectroscopy and X-ray Fluorescence elemental mapping experiments were performed at the TwinMic beamline of Elettra synchrotron facility (Trieste, Italy) [65–67]. The STXM images and the XRF maps were acquired with the beam energy set at 1 keV, except for Mg containing samples, where maps were acquired at 1.4 keV to be able to excite Mg as well. The micro-XAS spectra were calibrated with Mn^{2+}, Mn^{4+}, Cu^0, Co^0 and Ni^0 reference samples.

4. Conclusions

In this paper we studied the coelectrodeposition (CECD) of ternary Mn-based/polypyrrole (PPy) composites (Mn–Co–Cu/PPy, Mn–Co–Mg/PPy, Mn–Ni–Mg/PPy) for ORR electrocatalysis in alkaline aqueous ambients. The Mn–Co–Cu/PPy catalyst possess better electrocatalytic activity for $4e^-$ reduction of O_2 resulting more appealing for air cathode applications. The investigated electrodeposition conditions give rise to the growth of materials with morphology and elemental distribution that are homogeneous at the mesoscopic scale. The peculiar space patterns corresponding to the individual ternary systems are the result of the specific morphochemical couplings typical of the single chemistries and fit the scenarios found by analysis of a dynamic electrodeposition model recently developed in our group [41]. Micro-XAS at the Mn L-edge shows that the dominating species is Mn^{3+}, with smaller amounts of Mn^{4+}. As far as the chemical state of Mn is concerned, the systems studied in this paper are a notable improvement with respect to our previous studies on Mn/PPy and binary Mn–X/PPy electrodeposits, since with ternary materials the most active forms of Mn can be obtained directly in the as-prepared material. Co and Ni are present as a mixture of elemental and two-valent forms, resulting from the alternation of anodic and cathodic pulses in the CECD protocol and, for the same reason, Cu is found in both $Cu^{0,+}$ and Cu^{2+} forms. In conclusion, we can state that, thanks to the use of high-resolution XRF and XAS techniques, we achieved an insightful understanding of the chemical state and its space distribution in Mn-based ternary electrodeposited composites with PPy matrix and molecular aspects of the role of doping elements in electrocatalyst fabrication become accessible, contributing to knowledge-based material design and optimization.

Author Contributions

Benedetto Bozzini, Patrizia Bocchetta and Alessandra Gianoncelli have contributed equally to the different activities related to the research described in this paper, including: material preparation,

beamline operation, beamtime actions and electrochemical measurements. Moreover, all authors have equally contributed in elaborating the experimental data and writing the manuscript. All authors have given approval to the final version of the manuscript.

Conflicts of Interest

The authors declare no conflict of interest.

References

1. Yuan, X.; Ding, X.-L.; Wang, C.-Y.; Ma, Z.-F. Use of polypyrrole in catalysis for low temperature fuel cells. *Energy Environ. Sci.* **2013**, *6*, 1105–1124.
2. Nam, D.-H.; Lim, S.-J.; Kim, M.-J.; Kwon, H.-S. Facile synthesis of SnO_2-polypyrrole hybrid nanowires by cathodic electrodeposition and their application to Li-ion battery anodes. *RSC Adv.* **2013**, *3*, 16102–16108.
3. Rapecki, T.; Donten, M.; Stojek, Z. Electrodeposition of polypyrrole—Au nanoparticles composite from one solution containing gold salt and monomer. *Electrochem. Commun.* **2010**, *12*, 624–627.
4. Trueba, M.; Trasatti, S.P.; Trasatti, S. Electrocatalytic activity for hydrogen evolution of polypyrrole films modified with noble metal particles. *Mater. Chem. Phys.* **2006**, *98*, 165–171.
5. Andreoli, E.; Rooney, D.A.; Redington, W.; Gunning, R.; Breslin, C.B. Electrochemical Deposition of Hierarchical Micro/Nanostructures of Copper Hydroxysulfates on Polypyrrole_Polystyrene Sulfonate Films. *J. Phys. Chem. C* **2011**, *115*, 8725–8734.
6. Ilieva, M.; Tsakova, V. Copper modified poly(3,4-ethylenedioxythiophene) Part I. Galvanostatic experiments. *Synth. Metals* **2004**, *141*, 281–285.
7. Ilieva, M.; Tsakova, V. Copper modified poly(3,4-ethylenedioxythiophene) Part II. Potentiostatic experiments. *Synth. Metals* **2004**, *141*, 287–292.
8. Jung, Y.; Singh, N.; Choi, K.-S. Cathodic Deposition of Polypyrrole Enabling the One-Step Assembly of Metal-Polymer Hybrid Electrodes. *Angew. Chem. Int. Ed.* **2009**, *48*, 8331.
9. Kim, S.J.; Hong, M.K.; Chung, J.K.; Park, S.Y. Electrochemical properties of $Ni(OH)_2$/polypyrrole composite electrode prepared by electrodeposition for pseudo-capacitor. *J. Ceram. Process. Res.* **2013**, *13*, s274–s277.
10. Nam, D.H.; Kim, M.J.; Lim, S.J.; Kwon, H.S. Single-step synthesis of polypyrrole nanowires by cathodic electropolymerization. *J. Mater. Chem. A* **2013**, *1*, 8061–8068.
11. Nam, D.-H.; Lim, S.-J.; Kim, M.-J.; Kwon, H.-S. One-step synthesis of a Si/CNT-polypyrrole composite film by electrochemical deposition. *RSC Adv.* **2014**, *4*, 10212–10215.
12. Otero, T.F.; Boyano, I. Comparative study of Conductive Polymers by the ESCR Model. *J. Phys. Chem. B* **2003**, *107*, 6730–6738.
13. Bozzini, B.; Bocchetta, P.; Gianoncelli, A.; Mele, C.; Kiskinova, M. Electrodeposition of Co/CoO nanoparticles onto graphene for ORR electrocatalysis: A study based on micro-X-ray absorption spectroscopy and X-ray fluorescence mapping. *Acta Chim. Slov.* **2014**, *61*, 263–271.
14. Otero, T.F.; Costa, S.O.; Ariza, M.J.; Marquez, M. Electrodeposition of Cu on deeply reduced polypyrrole electrodes at very high cathodic potentials. *J. Mater. Chem.* **2005**, *15*, 1662–1667.

15. Bocchetta, P.; Gianoncelli, A.; Abyaneh, M.K.; Kiskinova, M.; Jezeršek, D.; Mele, C.; Bozzini, B. Electrosynthesis of Co/PPy nanocomposites for ORR electrocatalysis: A study based on quasi-*in situ* X-ray absorption, fluorescence and *in situ* Raman spectroscopy. *Electrochim. Acta* **2014**, *137*, 535–545.

16. Tsakova, V. How to affect number, size, and location of metal particles deposited in conducting polymer layers. *J. Solid State Electrochem.* **2008**, *12*, 1421–1434.

17. Bouzek, K.; Holzhauser, P.; Kodym, R.; Moravcova, S.; Paidar, M. Utilization of Nafion®/conducting polymer composite in the PEM type fuel cells. *J. Appl. Electrochem.* **2007**, *37*, 137–145.

18. Yang, C.H.; Wen, T.C. Electrodeposited platinum nanoparticles in a sulfonate-polyaniline film for the electrosorption of methanol and sorbitol. *Electrochim. Acta* **1998**, *44*, 207–218.

19. Chen, W.; Li, C.-M.; Yu, L.; Lu, Z.; Zhou, Q. *In situ* AFM study of electrochemical sythesis of polypyrrole/Au nanocomposite. *Electrochem. Commun.* **2008**, *10*, 1340–1434.

20. Guo, Z.; Shin, K.; Karki, A.B.; Young, D.P.; Kaner, R.B.; Hahn, H.T. Fabrication and characterization of iron oxide nanoparticles filled polypyrrole nanocomposites. *J. Nanopart. Res.* **2009**, *11*, 1441–1452.

21. Elliott, C.M.; Kopelove, A.B.; Albery, W.J.; Chen, Z. Nonaqueous electrochemistry of polypyrrole/polystyrenesulfonate composire films: Voltammetric, coulometric, EPR, and a.c. impedance studies. *J. Phys. Chem.* **1991**, *95*, 1743–1747.

22. Deng, J.; Peng, Y.; He, C.; Long, X.; Li, P.; Chan, A.S.C. Magnetic and conducting Fe_3O_4-polypyrrole nanoparticles with core shell structure. *Polym. Int.* **2003**, *52*, 1182–1187.

23. Ispas, A.; Peipmann, R.; Adolphi, B.; Efimov, I.; Bund, A. Electrodeposition of pristine and composite poly(3,4-ethylenedioxythiophene) layers studied by electro-acoustic impedance measurement. *Electrochim. Acta* **2011**, *56*, 3500–3506.

24. Ispas, A.; Peipmann, R.; Bund, A.; Efimov, I. On the P-doping of PEDOT layers in various ionic liquids studied by EQCM and acoustic impedance. *Electrochim. Acta* **2009**, *54*, 4668–4675.

25. Weidlich, C.; Mangold, K.M.; Jüttner, K. EQCN study of the ion exchange behaviour of polypyrrole with different counterions in differente electrolytes. *Electrochim. Acta* **2005**, *50*, 1547–1552.

26. El Mouahid, O.; Rakotondrainibe, A.; Crouigneau, V.; Léger, J.M.; Lamy, C.A. UV-visible study of the electropolymerization of CoTAPP at vitreous carbon and investigation of its catalytic activity towards the electroreduction of dioxygen. *J. Electroanal. Chem.* **1998**, *455*, 209–222.

27. Doherty, W.J., III; Wysocki, R.J., Jr.; Armstrong, N.R.; Saavedra, S.S. Potential-Modulated, Attenuated Total Reflectance Spectroscopy of Poly(3,4-ethylenedioxythiophene) and Poly(3,4-ethylenedioxythiophene Methanol) Copolymer Films on Indium-Tin Oxide. *J. Phys. Chem. B* **2006**, *110*, 4900–4907.

28. Giacomini, M.T.; de Souza, L.M.M.; Ticianelli, E.A. Spectroscopic ellipsometry investigation of the redox process of polypyrrole in several aqueous solutions. *Surf. Sci.* **1998**, *409*, 465–473.

29. Ferreira, C.A.; Domenech, S.C.; Lacaze, P.C. Synthesis and characterization of polypyrrole/TiO_2 composites on mild steel. *J. Appl. Electrochem.* **2001**, *31*, 49–56.

30. Luo, X.J.; Xia, W.B.; Gao, J.L.; Zhang, S.Y.; Li, Y.L.; Tang, S.L.; Du, Y.W. Enhanced magnetic performance of metal-organic nanowire arrays by FeCo/polypyrrole co-electrodeposition. *J. Appl. Phys.* **2013**, *113*, 17B908.

31. Montoya, P.; Jaramillo, F.; Calderón, J.; de Torresi, S.C.; Torresi, R. Evidence of redox interactions between polypyrrole and Fe_3O_4 in polypyrrole-Fe_3O_4 composite films. *Electrochim. Acta* **2010**, *55*, 6116–6122.

32. Watanabe, N.; Morais, J.; Accione, S.B.B.; Morrone, Â.; Schmidt, J.E.; Martins Alves, M.C. Electronic, Structural, and Magnetic Properties of Cobalt Aggregates Embedded in Polypyrrole. *J. Phys. Chem. B* **2004**, *108*, 4013–4017.

33. Zu, T.M.; Yen, S.J.; Chen, E.C.; Sung, T.W.; Chiang, R.K. Conducting and magnetic behaviors of monodispersed iron oxide/polypyrrole nanocomposites synthesized by *in situ* chemical oxidative polymerization. *J. Polym. Sci. A* **2007**, *45*, 4647–4655.

34. Malik, M.A.; Kuleszka, P.J.; Wlodarczyk, R.; Wittstock, G.; Szargan, R.; Bala, H.; Galus, Z. Formation of ultra-thin prussian blue layer of carbon steel that promotes adherence of hybrid polypyrrole based protective coating. *J. Solid State Electrochem.* **2005**, *9*, 403–411.

35. Li, S.; Qiu, Y.; Guo, X. Comparison of PPy/sulphate-copper complexes synthesized by the pulse method and the traditional DC method. *React. Funct. Polym.* **2009**, *69*, 743–749.

36. Ikeda, O.; Okabayashi, K.; Tamura, H. Electrocatalytic reduction of oxygen on cobalt-doped polypyrrole films. *Chem. Lett.* **1983**, *12*, 1821–1824.

37. Masa, J.; Schilling, T.; Bron, M.; Schumann, W. Electrochemical synthesis of metal-polypyrrole composites and their activation for electrocatalytic reduction of oxygen by thermal treatement. *Electrochim. Acta* **2012**, *60*, 410–418.

38. Chipara, M.; Skomski, R.; Sellmyer, D.J. Electrodeposition and magnetic properties of polypyrrole-Fe nanocomposites. *Mater. Lett.* **2007**, *61*, 2412–2415.

39. Haseko, Y.; Shrestha, N.K.; Teruyama, S.; Saji, T. Reversal pulsing electrodeposition of Ni/polypyrrole composite film. *Electrochim. Acta* **2006**, *51*, 3652–3657.

40. Bozzini, B.; Bocchetta, P.; Gianoncelli, A.; Kourousias, G.; Kiskinova, M.; dal Zilio, S. *In situ* soft X-ray fluorescence and absorption microspectroscopy: A study of Mn–Co/polypyrrole electrodeposition. *J. Vac. Sci. Technol. A* **2015**, in press.

41. Gianoncelli, A.; Sgura, I.; Bocchetta, P.; Lacitignola, D.; Bozzini, B. High-lateral resolution X-ray fluorescence microspectroscopy and dynamic mathematical modelling as tools for the study of electrodeposited electrocatalysts. *X-RAY Spectrom.* **2015**, in press.

42. Bozzini, B.; Gianoncelli, A.; Bocchetta, P.; dal Zilio, S.; Kourousias, G. Fabrication of a sealed electrochemical microcell for *in situ* soft X-ray microspectroscopy and testing with *in situ* Co-polypyrrole composite electrodeposition for Pt-free oxygen electrocatalysis. *Anal. Chem.* **2014**, *86*, 664–670.

43. Caramia, V.; Bozzini, B. Materials-science aspects of Zinc—Air batteries: A review. *Mater. Renew. Sustain. Energy* **2014**, *3*, 1–12.

44. Bocchetta, P.; Amati, M.; Bozzini, B.; Catalano, M.; Gianoncelli, A.; Gregoratti, A.; Taurino, A.; Kiskinova, M. Quasi-*in-situ* Single-Grain Photoelectron Microspectroscopy of Co/PPy Nanocomposites under Oxygen Reduction Reaction. *ACS Appl. Mater. Interfaces* **2014**, *6*, 19621–19629.

45. Bashyam, R.; Zelenay, P. A class of non-precious metal composite catalysts for fuel cells. *Nature* **2006**, *443*, 63–66.

46. Dias, H.V.R.; Fianchini, M.; Rajapakse, R.M.G. Greener Method for High-Quality Polypyrrole. *Polymer* **2006**, *47*, 7349–7354.

47. Nguyen-Cong, H.; El-Abbassi, K.; Gautier, J.L.; Chartier, P. Oxygen reduction on oxide/polypyrrole composite electrodes: Effect of doping anions. *Electrochim. Acta* **2005**, *50*, 1369–1376.

48. An, K.H.; Jeon, K.K.; Heo, J.K.; Lim, S.C.; Bae, D.J.; Lee, Y.H. High-capacitance supercapacitor using a nanocomposite electrode of single-walled carbon nanotube and polypyrrole. *J. Electrochem. Soc.* **2002**, *149*, A1058–A1062.

49. Sadki, S.; Schottland, P.; Brodie, N.; Sabouraud, G. The mechanisms of pyrrole electropolymerization. *Chem. Soc. Rev.* **2000**, *29*, 283–293.

50. Vondrák, J.; Klápště, B.; Velická, J.; Sedlaříková, M.; Novák, V.; Reiter, J. Electrochemical Activity of Manganese Oxide/Carbon-based Electrocatalysts. *J. New Mater. Electrochem. Syst.* **2005**, *8*, 209–212.

51. Vondrák, J.; Klápště, B.; Velická, J.; Sedlaříková, M.; Novák, V.; Reiter, J. Carbon/Manganese oxide based fuel cell electrocatalyst using "flywheel" principle. *J. New Mater. Electrochem. Syst.* **2005**, *8*, 1–4.

52. Mao, L.; Zhang, D.; Sotomura, T.; Nakatsu, K.; Koshiba, N.; Ohsaka, T. Mechanistic study of the reduction of oxygen in air electrode with manganese oxides as electrocatalysts. *Electrochim. Acta* **2003**, *48*, 1015–1021.

53. Roche, I.; Scott, K. Carbon-supported manganese oxide nanoparticles as electrocatalysts for oxygen reduction reaction (ORR) in neutral solution. *J. Appl. Electrochem.* **2008**, *39*, 197–204.

54. Cao, R.; Lee, J.-S.; Liu, M.; Cho, J. Recent Progress in Non-Precious Catalysts for Metal-Air Batteries. *Adv. Energy Mater.* **2012**, *2*, 816–829.

55. Zhang, G.Q.; Zhang, X.G.; Wang, Y.G. A new air electrode based on carbon nanotubes and Ag-MnO_2 for metal air electrochemical cells. *Carbon* **2004**, *42*, 3097–3102.

56. Bard, A.J. Faulkner, L.R. *Electrochemical Methods: Fundamentals and Applications*; John Wiley & Sons: New York, NY, USA, 2001; pp. 335–344.

57. Davis, R.E.; Horvath, G.L.; Tobias, C.W. The solubility and diffusion coefficient of oxygen in potassium hydroxide solutions. *Electrochim. Acta* **1967**, *12*, 287–297.

58. De Koninck, M.; Marsan, B. $Mn_xCu_{1-x}Co_2O_4$ used as bifunctional electrocatalyst in alkaline medium. *Electrochim. Acta* **2008**, *53*, 7012–7021.

59. Liang, Y.; Li, Y.; Wang, H.; Zhou, J.; Wang, J.; Regier, T.; Dai, H. Co_3O_4 nanocrystals on graphene as a synergistic catalyst for oxygen reduction reaction. *Nat. Mater.* **2011**, *10*, 780–786.

60. Lima, F.H.B.; Calegaro, M.L.; Ticianelli, E.A. Investigations of the catalytic properties of manganese oxides for the oxygen reduction reaction in alkaline media. *J. Electroanal. Chem.* **2006**, *590*, 152–160.

61. Lima, F.H.B.; Calegaro, M.L.; Ticianelli, E.A. Electrocatalytic activity of manganese oxides prepared by thermal decomposition for oxygen reduction. *Electrochim. Acta* **2007**, *52*, 3732–3738.

62. Benedetto, B.; Lacitignola, D.; Sgura, I. Spatio-Temporal Organisation in Alloy Electrodeposition: A Morphochemical Mathematical Model and its Experimental Validation. *J. Solid State Electrochem.* **2013**, *17*, 467–479.

63. Lacitignola, D.; Bozzini, B.; Sgura, I. Spatio-temporal organization in a morphochemical electrodeposition model: Hopf and Turing instabilities and their interplay. *Eur. J. Appl. Math.* **2015**, *26*, 143–173.

64. Wang, J.; Wang, K.; Wang, F.-B.; Xia, X.-H. Bioinspired copper catalyst effective for both reduction and evolution of oxygen. *Nat. Commun.* **2014**, *5*, doi:10.1038/ncomms6285.

65. Kaulich, B.; Susini, J.; David, C.; di Fabrizio, E.; Morrison, G.; Charalambous, P.; Thieme, J.; Wilhein, T.; Kovac, J.; Bacescu, D.; *et al. Proceedings of 8th International Conference X-ray Microscopy*; Aoki, S., Kagoshima, Y., Suzuki, Y., Eds.; IPAP: Tokyo, Japan, 2005; Volume 7, pp. 22–25.

66. Kaulich, B.; Thibault, P.; Gianoncelli, A.; Kiskinova, M. Transmission and emission X-ray microscopy: Operation modes, contrast mechanisms and applications. *J. Phys. Condensed Matter* **2011**, *23*, doi:10.1088/0953-8984/23/8/083002.

67. Gianoncelli, A.; Kaulich, B.; Alberti, R.; Klatka, T.; Longoni, A.; de Marco, A.; Marcello, A.; Kiskinova, M. Simultaneous soft X-ray transmission and emission microscopy. *Nuclear. Intrum. Methods Phys. Res. Sect. A* **2009**, *608*, 195–198.